Our data now provide evidence for a function for Eph receptors and ephrins that establishes roles in NMDA-independent forms of synaptic plasticity.

Our results provide strong support for postsynaptic induction of mossy fiber LTP and are consistent with earlier reports in which tetanic stimulation elicited postsynaptic rises in calcium, triggering induction of LTP (*3*, *5*). Furthermore, we have identified a retrograde signaling pathway, EphB receptor–ephrin B ligand interaction, that links postsynaptic induction with presynaptic expression of long-term changes in release probability. These results suggest a model for induction of mossy fiber LTP initiated by activation of kainate and/or metabotropic glutamate receptors upon tetanic stimulation of mossy fibers (*3*, *32*, *33*) and subsequent postsynaptic intracellular signaling, resulting in the promotion of clustering of EphB receptors by GRIP or a similar molecule. This interaction allows EphRs to associate with and activate reverse signaling by presynaptic ephrin-B ligands, which may then regulate downstream events, including those mediated by PKA, and ultimately results in an increase in glutamate release in mossy fiber terminals.

References and Notes

1. M. G. Weisskopf, R. A. Nicoll, *Nature* **376**, 256 (1995).
2. Z. Xiang, A. C. Greenwood, E. W. Kairiss, T. H. Brown, *J. Neurophysiol.* **71**, 2552 (1994).
3. M. F. Yeckel, A. Kapur, D. Johnston, *Nature Neurosci.* **2**, 625 (1999).
4. J. Mellor, R. A. Nicoll, *Nature Neurosci.* **4**, 125 (2001).
5. S. Williams, D. Johnston, *Neuron* **3**, 583 (1989).
6. R. A. Zalutsky, R. A. Nicoll, *Science* **248**, 1619 (1990).
7. H. Katsuki, S. Kaneko, A. Tajima, M. Satoh, *Neurosci. Res.* **12**, 393 (1991).
8. Materials and methods are available as supporting material on *Science* Online.
9. M. I. Daw *et al.*, *Neuron* **28**, 873 (2000).
10. C. H. Kim, H. J. Chung, H. K. Lee, R. L. Huganir, *Proc. Natl. Acad. Sci. U.S.A.* **98**, 11725 (2001).
11. S. Matsuda, S. Mikawa, H. Hirai, *J. Neurochem.* **73**, 1765 (1999).
12. H. J. Chung, J. Xia, R. H. Scannevin, X. Zhang, R. L. Huganir, *J. Neurosci.* **20**, 7258 (2000).
13. R. Klein, *Curr. Opin. Cell Biol.* **13**, 196 (2001).
14. M. T. Moreno-Flores, F. Wandosell, *Neuroscience* **91**, 193 (1999).
15. R. Torres *et al.*, *Neuron* **21**, 1453 (1998).
16. H. Dong *et al.*, *Nature* **386**, 279 (1997).
17. S. Srivastava *et al.*, *Neuron* **21**, 581 (1998).
18. A. Contractor *et al.*, data not shown.
19. S. J. Holland *et al.*, *Nature* **383**, 722 (1996).
20. K. Bruckner, E. B. Pasquale, R. Klein, *Science* **275**, 1640 (1997).
21. Q. Lu, E. E. Sun, R. S. Klein, J. G. Flanagan, *Cell* **105**, 69 (2001).
22. C. A. Cowan, M. Henkemeyer, *Nature* **413**, 174 (2001).
23. E. Stein *et al.*, *Genes Dev.* **12**, 667 (1998).
24. Y. Y. Huang, X. C. Li, E. R. Kandel, *Cell* **79**, 69 (1994).
25. M. G. Weisskopf, P. E. Castillo, R. A. Zalutsky, R. A. Nicoll, *Science* **265**, 1878 (1994).
26. N. W. Gale *et al.*, *Neuron* **17**, 9 (1996).
27. M. Henkemeyer *et al.*, *Cell* **86**, 35 (1996).
28. M. B. Dalva *et al.*, *Cell* **103**, 945 (2000).
29. J. T. Henderson *et al.*, *Neuron* **32**, 1041 (2001).
30. I. C. Grunwald *et al.*, *Neuron* **32**, 1027 (2001).
31. M. A. Takasu, M. B. Dalva, R. E. Zigmond, M. E. Greenberg, *Science* **295**, 491 (2002).
32. Z. A. Bortolotto *et al.*, *Nature* **402**, 297 (1999).
33. A. Contractor, G. Swanson, S. F. Heinemann, *Neuron* **29**, 209 (2001).
34. H. Kamiya, H. Shinozaki, C. Yamamoto, *J. Physiol.* **493**, 447 (1996).

35. This work was supported by grants from the NIH National Institute of Mental Health (A.C., M.H.), National Alliance for Research on Schizophrenia and Depression (C.R., G.T.S.) and NIH National Institute of Neurological Disorders and Stroke (S.F.H.). We thank W. Che for technical assistance and R. Allen for generating His-GRIP protein.

Supporting Online Material

www.sciencemag.org/cgi/content/full/296/5574/1864/DC1

Materials and Methods

17 December 2001; accepted 26 April 2002

Two-Photon Imaging of Lymphocyte Motility and Antigen Response in Intact Lymph Node

Mark J. Miller,[1] Sindy H. Wei,[1] Ian Parker,[2]* Michael D. Cahalan[1]*†

Lymphocyte motility is vital for trafficking within lymphoid organs and for initiating contact with antigen-presenting cells. Visualization of these processes has previously been limited to in vitro systems. We describe the use of two-photon laser microscopy to image the dynamic behavior of individual living lymphocytes deep within intact lymph nodes. In their native environment, T cells achieved peak velocities of more than 25 micrometers per minute, displaying a motility coefficient that is five to six times that of B cells. Antigenic challenge changed T cell trajectories from random walks to "swarms" and stable clusters. Real-time two-photon imaging reveals lymphocyte behaviors that are fundamental to the initiation of the immune response.

The process by which lymphocytes transit through organized lymphoid tissues is crucial to the immune response, but it has not been amenable to direct experimental investigation and remains poorly understood (*1*). During transit, T lymphocytes can encounter antigen-presenting cells (APCs), take up residence in specific regions of lymphoid tissue, or reenter the circulation. In vivo studies at a macroscopic level with cannulated lymphatic vessels have provided population measurements of lymphocyte recirculation under physiological conditions (*1*). At the cellular and molecular level, our understanding of the immune response has been greatly enhanced by studies of cultured lymphocytes in artificial two- and three-dimensional (3D) systems (*2*, *3*). In vitro systems, however, cannot replicate local environmental factors within intact lymphoid organs that shape the antigen recognition process, the transit of lymphocytes through the tissue, and the development of subsequent effector functions (*4*). To bridge this gap between in vivo and in vitro approaches, we used two-photon microscopy (*5*, *6*) to image individual living T and B lymphocytes deep within the intact lymph node.

Purified T and B cells from donor BALB/c mice were labeled with green [5- (and 6-) carboxyfluorescein diacetate succininyl ester (CFSE)] or red (5-(and-6)-(((4-chloromethyl) benzoyl)amino)tetramethylrhodamine) (CMTMR)] fluorescent dyes and injected into the tail vein of recipient mice (*7*). Subsequent two-photon imaging (*8*) of isolated, superfused lymph nodes showed the expected localization of B cells within primary follicles and of T cells predominantly in the interfollicular spaces of the diffuse cortex (Fig. 1, A and B). Individual cells could be resolved and tracked to depths of up to 350 μm beneath the capsular surface (Fig. 1, C and D), and their differing morphologies were readily distinguished (Fig. 1, E and F). In other experiments, lymph nodes were prestained with CMTMR to visualize the distribution of CFSE-stained T cells with respect to the reticular fiber network (Fig. 1G) (3D rotation is shown in Movie S1).

Dynamic changes in the locomotion of T and B cells were tracked with time-lapse 3D imaging. At room temperature, lymphocytes were nonmotile and spherical, but on warming they adopted polarized shapes and moved with velocities that were steeply dependent on temperature and were maximal near the physiological body temperature (Movie S2). Most T cells progressed by a series of repeated lunges, becoming elongated while moving rapidly and balling up when paused (Fig. 2, A and C; Movie S3). In contrast, B cells followed mean-

[1]Department of Physiology and Biophysics, [2]Department of Neurobiology and Behavior, University of California, Irvine, CA 92697–4561, USA.

*These authors contributed equally to this work.
†To whom correspondence should be addressed. E-mail: mcahalan@uci.edu

dering paths at relatively constant velocity and displayed a compact triangular morphology, with filopodial processes constantly forming and retracting (Fig. 2, B and D). The mean velocity of T cells (10.8 ± 0.1 μm min^{-1}, 43 cells, 3277 measurements) was nearly double that of B cells (6.4 ± 0.07 μm min^{-1}, 38 cells, 3251 measurements), and the distribution of T cell velocities was broader and more skewed, with velocities >25 μm min^{-1} observed (Fig. 2, C and D). T cells found within follicles retained their characteristic motility pattern. Several less frequent patterns of T cell motility and shape were also evident, including rapidly moving cells with torpedo shapes, cells that were attached to structures by long membrane tethers, and cells that were relatively stationary but exhibited probing behavior (Fig. 2, E through G). These diverse patterns of behavior suggest that the lymphocytes were interacting with unseen elements in their environment; for example, visualization of the reticular fiber network with CMTMR revealed T cells adhering to, but not crawling along, these fibers (Movie S4).

Most T cells preferentially moved parallel to the overlying capsule. Motion perpendicular to the capsule appeared as gradual drift or more rapid movement through "portals." In the *xy* plane, T cells characteristically moved in a consistent direction for short (1- to 3-min) periods; but over longer times, the tracks of both T and B cells appeared random, with T cells exploring a much wider territory on average than B cells (Fig. 3, A and B). The mean absolute displacement of T and B cells from their origin increased proportionally with the square root of time (Fig. 3, C and D), indicating that both cell types use a random-walk search strategy within the lymph node. The mean displacement of cells as a function of time can thus be characterized in terms of a "motility coefficient" (analogous to a diffusion coefficient), with values of 67 and 12 μm^2 min^{-1} for T and B cells, respectively. The larger territory covered by T cells arises from both their greater mean velocity and their longer mean free path length (distance traveled in a straight line before turning).

We next investigated the effects of antigen stimulation, using CFSE to track both motility and proliferation of antigen-specific DO11.10 T cells in the lymph node (*9*, *10*). Antigenic challenge followed by transfer of antigen-specific T cells resulted in T cell enlargement on day 1 and subsequently led to several rounds of cell division by day 5 (Fig. 4, A through C). In control lymph nodes from unprimed mice, almost all DO11.10 T cells were freely motile (mean velocity, 12.24 ± 0.09 μm min^{-1}; 197 cells; 9811 measurements), like BALB/c T cells, and followed meandering paths uniformly distributed throughout the entire imaging field (Fig. 4D and Movie S5A). In contrast, 1 day after adoptive transfer into antigen-challenged animals, antigen-specific T cells displayed two distinct behaviors. Some formed tight clusters of relatively stationary cells, many of which were enlarged to a diameter of ~1.5 times that of control cells from unprimed mice (Fig. 4E and Movies S5B and S6). Freely motile cells that encountered such clusters usually stuck but sometimes dissociated and again moved freely. Other groups of T cells were yet further enlarged (with diameters about double those of control cells) and massed in "swarms," looping within regions a few tens of micrometers across (Fig. 4F and Movie S5C). The proportion of stationary cells (velocities <2 μm min^{-1}) increased from 3% in control nodes to 25% in antigen-primed nodes. Five days after antigen priming, T cells of varying intensity were observed, corresponding to nondivided and divided cells, and these populations displayed different motility patterns (Fig. 4G and Movie S5D). Brightly stained nondivided T cells moved freely with a velocity (12.03 ± 0.7 μm min^{-1}, 96 cells, 3028 measurements) almost identical to that seen in unprimed control mice. Dim cells (cells that had divided three or more times) displayed clusters with more stationary cells than those in the nondivided population (21 versus 10%), but the motile divided cells displayed mean velocities similar to those of the nondivided population or of unprimed controls.

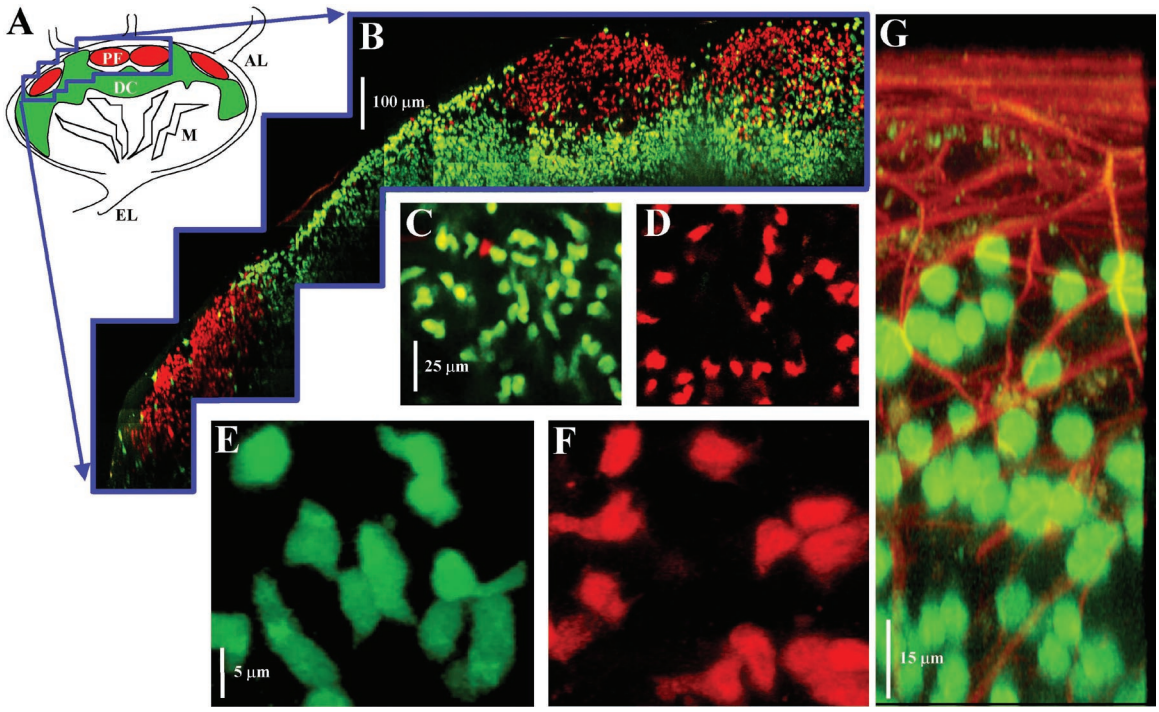

Fig. 1. Two-photon imaging of living T and B lymphocytes deep within an intact isolated lymph node. (**A**) Schematic diagram of a lymph node, illustrating primary follicles (PF), diffuse cortex (DC), medulla (M), afferent lymphatics (AL), and efferent lymphatics (EL). (**B**) Corresponding to the region outlined in (A), two-photon images within an inguinal lymph node at 36°C show CFSE-labeled living T cells (green) and CMTMR-labeled living B cells (red). Control experiments with inverse staining showed no differences in cell localization or motility. The image montage represents an optical cross section ("side" view) formed from maximum-intensity projections along the *x* axis from stacks of 350 image planes (200 μm by 200 μm) acquired at 1-μm *z* increments into the node. (**C** and **D**) Enlarged views illustrating the distribution of T cells in the diffuse cortex and B cells in a primary follicle, respectively. The appropriate homing of T and B cells is visible, as well as the variety of cell shapes. Images show maximum-intensity projections along the *z* axis ("top" view), formed from stacks of 17 planes acquired at 3-μm *z*-axis increments. (**E** and **F**) High-magnification images demonstrating the resolution of the fine cellular structure of individual T cells (~140-μm depth in diffuse cortex) and B cells (~50-μm depth in a primary follicle). (**G**) T cells stained with CFSE within the reticular fiber network stained with CMTMR (imaged at room temperature).

Live tissue imaging provides a window into the dynamic nature of lymphocyte behavior in the intact lymph node. Despite the densely packed cellular and fibrous matrix within the node, average and peak velocities of T and B cells within the intact lymph node are higher than those previously measured from in vitro studies (*11*–*15*). The overall motion parallel to the capsule is well described as a random walk, rather than directed movement in response to sustained chemokine gradients or along structural pathways. Although we cannot exclude the possibility that orientation signals derived

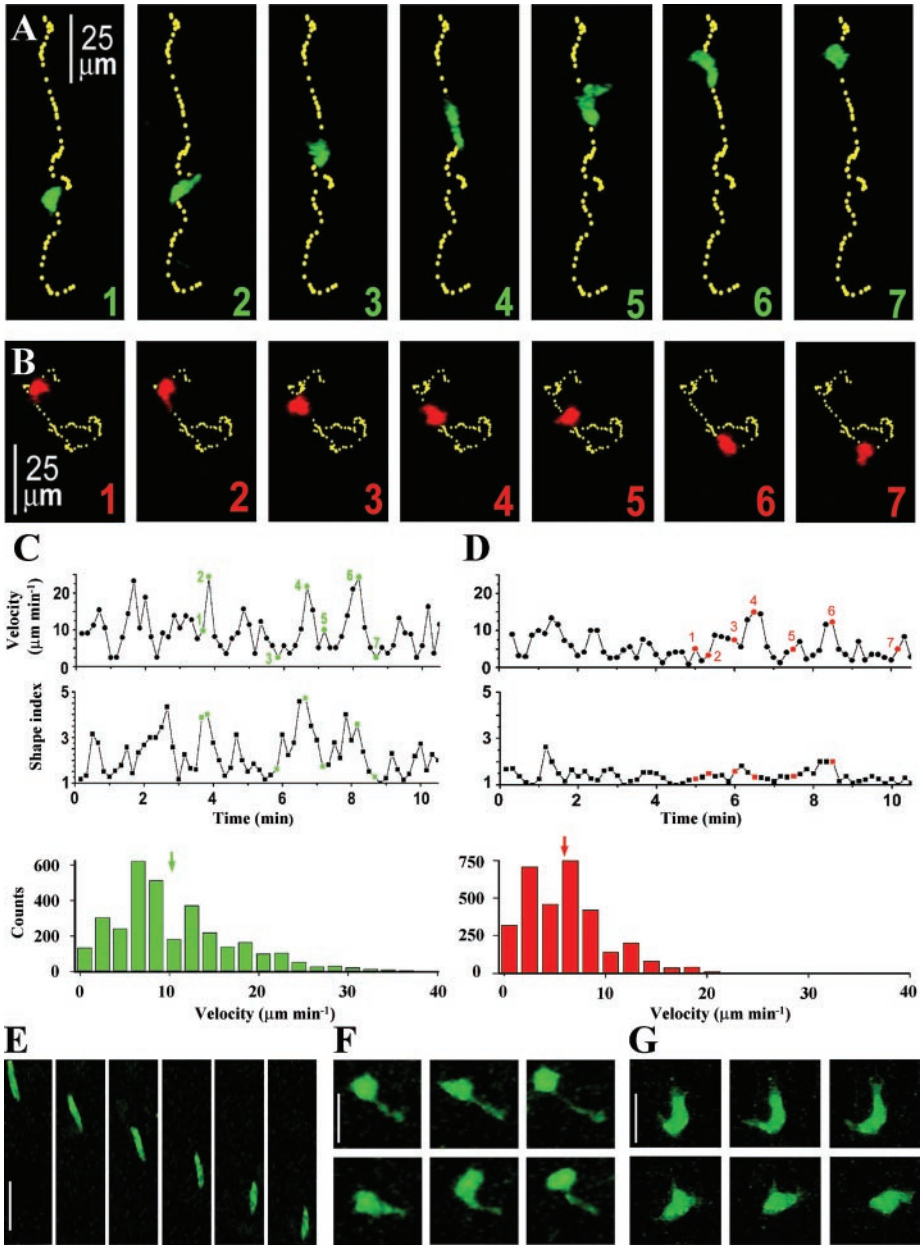

Fig. 2. Morphology and motility of BALB/c CD3$^+$ T and naïve B cells in inguinal and cervical lymph nodes. Image volumes of 200 μm by 200 μm by 50 μm (*xyz*) were acquired at 10-s intervals and then collapsed as maximum-intensity projections along the *z* axis for display and measurement. The imaging volume contained 25 to 100 labeled cells, in addition to a much larger unlabeled population from the recipient mouse. All motility experiments were performed at 36°C. Lymphocytes remained highly motile for >8 hours within the superfused nodes and could be continuously imaged for up to 1 hour without impairment. Quantitative measurements of T and B cell velocities, shapes, and trajectories were made by tracking the movements of individual cells in the *xy* plane (parallel to the overlying capsule) through stacks of 3D time-lapse images. (**A** and **B**) Image sequences illustrating typical T and B cell motility patterns, respectively. Yellow dots mark the positions of each cell at successive 10-s intervals. (**C**) Changes in the instantaneous cell velocity of the T cell shown in (A) are plotted along with corresponding measurements of the cell shape index (long axis divided by short axis). The histogram shows the distribution of T cell velocities, with a mean velocity indicated by the green arrow. (**D**) Corresponding velocities and shape indices for B cells, showing less variation than T cells and a lower overall mean velocity (red arrow). (**E** to **G**) Image sequences illustrating diverse modes of T cell motility and morphology: torpedo-like motion (E), tethered cell (F), and probing mode with numerous filopodial extensions (G). Scale bars, 20 μm in (E); 10 μm in (F) and (G).

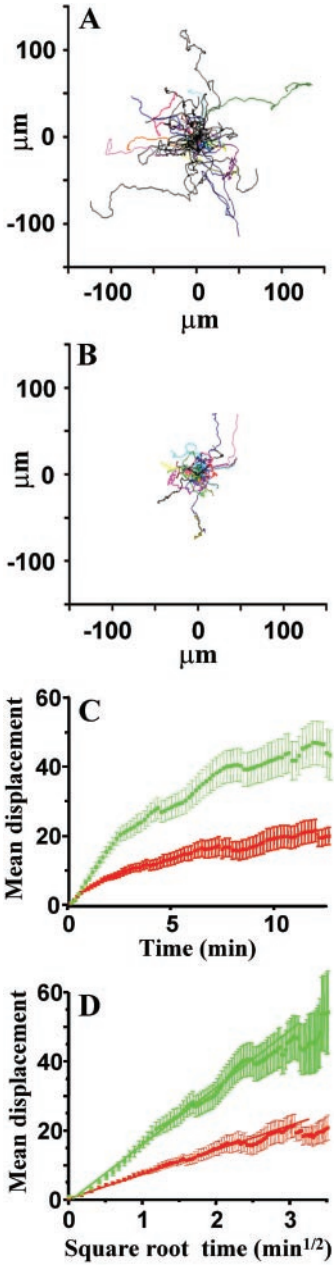

Fig. 3. T and B cells move within the lymph node by a random walk. (**A**) Superimposed tracks of 43 T cells in the diffuse cortex, normalized to their starting coordinates. (**B**) Corresponding tracks of 41 B cells in a primary follicle. (**C**) Mean displacement plot for T (green) and B (red) cells from (A) and (B). (**D**) The data from (C), replotted as a function of the square root of time. Points fall on straight lines, consistent with random movement, and the slope of each line represents the motility coefficient *M*, given by $M = x^2/4t$, where x = mean distance from origin at time t.

from the physiological blood and lymph flow and innervation are lost after isolation of the organ, it is noteworthy that T cell areas in the node are compartmentalized and isolated from the bulk flow of lymph or blood (*16*). T cells and APCs bearing the appropriate antigen must find each other in an immense landscape of extraneous cells. The increased range of T cell roaming relative to that of B cells may thus be an important aspect of their antigen search strategy, as compared to the very different requirements of B cells to receive T cell help within the more confined follicle. T cells exhibited behaviors (including abrupt changes in shape, velocity, and direction) that suggest interactions as they explore the environment. Furthermore, antigenic challenge dramatically alters the behavior of T cells, which become organized as both stationary clusters and dynamic swarms, suggesting that both stable and transient interactions between T cells and APC may have physiological importance for T cell activation. The static and swarming behaviors may reflect progressive stages of a single activation program or two parallel activation programs. We favor the former model, because T cell activation causes a progressive increase in cell size before division (*17*), and the enlarged size of cells in swarms thus suggests the following sequence of events: Initially, highly motile T

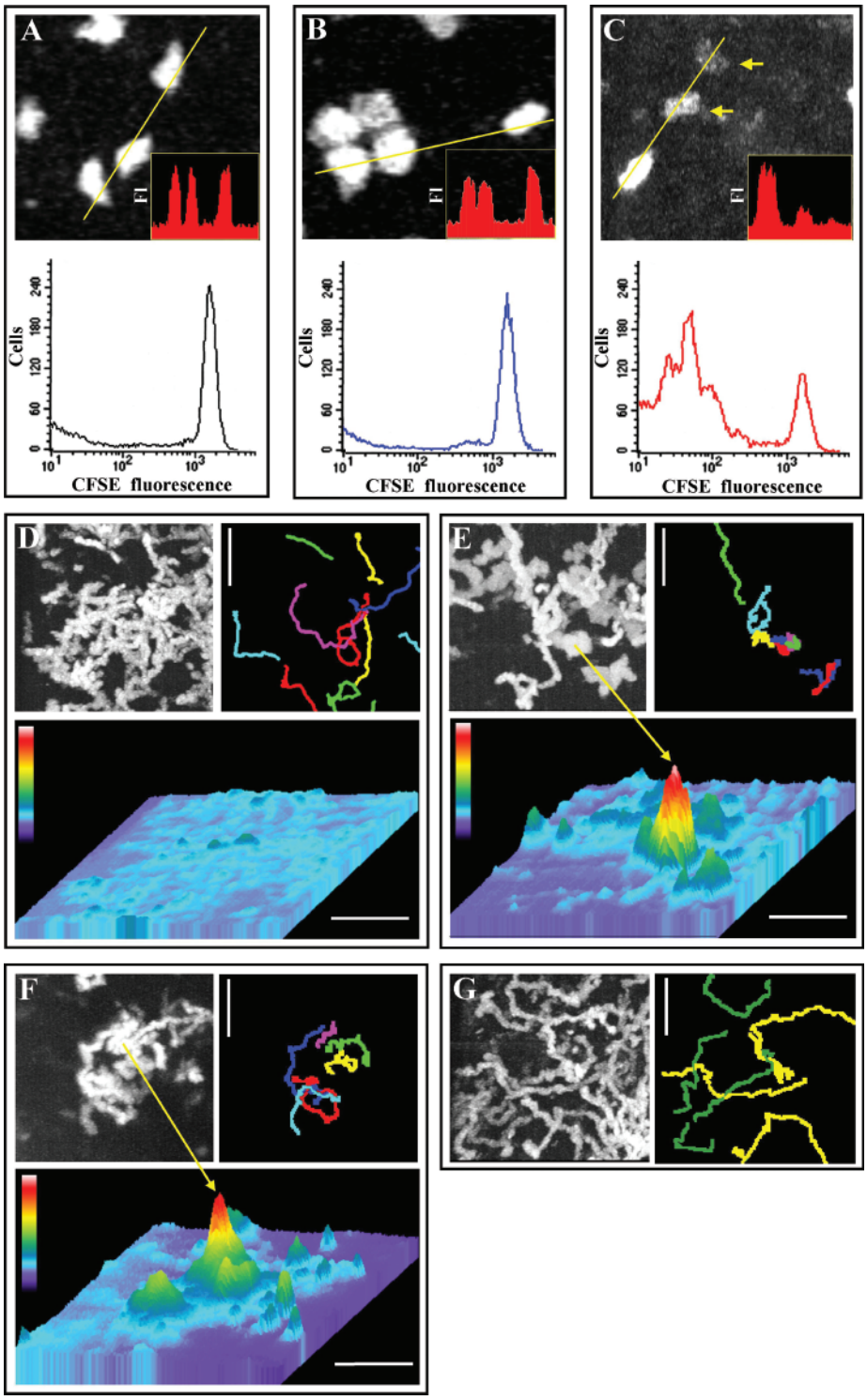

Fig. 4. Antigenic challenge alters T cell morphology and behavior. DO11.10 T cells specific for ovalbumin were transferred into recipient BALB/c mice challenged with subcutaneous ovalbumin and examined 1 and 5 days after adoptive transfer. The brightness and stability of CFSE labeling facilitated the tracking of cell trajectories within the tissue and permitted the history of proliferation after antigenic challenge to be determined. (**A** to **C**) T cell images within the lymph node with line-scan fluorescence intensities (FI) along the yellow line plotted in red (top), and flow cytometry analysis (bottom) of control unprimed mice (A) and primed mice 1 day (B) and 5 days (C) after transfer. In primed mice, many enlarged cells were seen on day 1, but very few had divided. On day 5, bright cells and dim cells (indicated by arrows) were seen within the lymph node, and flow cytometry revealed multiple rounds of cell division. (**D** to **G**) Analysis of motility patterns for DO11.10 T cells in nodes from an unprimed mouse (D) and from antigen-primed mice 1 day [(E) and (F)] and 5 days (G) after adoptive transfer of cells. In each panel, motility is displayed as a maximum-intensity superposition of 60 time-lapse images (top left); as representative tracks of individual cells (top right); and as contour plots (bottom) formed by summing the time-lapse images, where increasingly "warm" colors and higher elevations represent the increasing dwell time of cells at particular locations. Scale bars, 50 μm. In (D), the control, unprimed node is shown 5 days after adoptive transfer, displaying T cell paths that meandered uniformly throughout the field. The relatively flat contour plot further illustrates lack of clustering. T cell motility did not vary in control nodes examined 1 to 5 days after adoptive transfer. In (E), a tight cluster of relatively immobile T cells (indicated by arrow) in an antigen-primed mouse is shown 1 day after adoptive transfer. In (F), a representative example of a swarm of T cells (marked by arrow) is seen in an antigen-primed mouse 1 day after adoptive transfer. In (G), motility patterns of nondivided T cells (evident as bright traces in the superimposed image and marked as the four yellow cell tracks on the right) and divided cells (marked as the four green cell tracks) are seen in an antigen-primed mouse 5 days after adoptive transfer. Nondivided cells showed motility patterns and velocities similar to those in control, unprimed nodes; most divided cells were also highly motile. No contour plot is shown, because bright undivided cells would be overrepresented.

cells make contact with an APC, arrest, and depolarize, forming a small cluster as cells accumulate; subsequently, the clustered cells enlarge and begin to swarm before they undergo cell division.

This report introduces two-photon microscopy as a powerful tool for immunological studies that permits noninjurious imaging of individual living immune cells deep within highly scattering tissues. In addition to providing 3D resolution of cell morphology and permitting tracking of cell motility with a time resolution of a few seconds, successive cycles of cell division can be followed by means of the serial dilution of fluorescent label. The techniques described here may be applicable to other tissues (such as the thymus, spleen, and sites of inflammation), to other cell types (including APCs), to intravital imaging within intact organs, and to the use of fluorescent probes that signal cell function (such as Ca^{2+} signaling and gene expression).

References and Notes

1. A. J. Young, *Semin. Immunol.* **11**, 73 (1999).
2. S. K. Bromley *et al.*, *Annu. Rev. Immunol.* **19**, 375 (2001).
3. M. L. Dustin, A. R. de Fougerolles, *Curr. Opin. Immunol.* **13**, 286 (2001).
4. M. K. Jenkins *et al.*, *Annu. Rev. Immunol.* **19**, 23 (2001).
5. Q. T. Nguyen, N. Callamaras, C. Hsieh, I. Parker, *Cell Calcium* **30**, 383 (2001).
6. W. Denk, K. Svoboda, *Neuron* **18**, 351 (1997).
7. BALB/c $CD3^+$ T lymphocytes from peripheral lymph nodes and naïve BALB/c $CD19^+$ B lymphocytes from the spleen were enriched by negative selection to >98% purity by magnetic depletion using anti–MHC II MicroBeads (MHC, major histocompatibility complex) or anti-CD43 MicroBeads, respectively (Miltenyi Biotec, Auburn, CA). For purification of DO11.10 $CD3^+$ T cells, a combination of anti–MHC II MicroBeads and DX5 anti–natural killer cell MicroBeads was used as above. Cells were stained for 30 min at 37°C with 2 μM CFSE or CMTMR, destained, and washed with serum-free medium. Cells were resuspended in phosphate-buffered saline and adoptively transferred by tail vein injection into recipient BALB/c mice 4 to 6 weeks of age. For cell-tracking experiments, 10 million to 12 million purified CFSE-labeled T or B lymphocytes were adoptively transferred. Lymph nodes were harvested from the recipient mice 18 to 20 hours after adoptive transfer and were mounted in the imaging chamber. To observe the reticular fiber network, we counterstained lymph nodes in 2 μM CMTMR in serum-free medium for 45 min at room temperature and then destained and washed them. The labeling was stable for at least 1 hour under our imaging conditions.
8. Two-photon imaging was done with a custom-built, video-rate multiphoton microscope (*5*), using an upright Olympus BX50 microscope fitted with a ×20 water-immersion objective (numerical aperture = 0.95), a Spectra-Physics Tsunami femtosecond laser, and a resonant-mirror scan head. Image acquisition, a *z*-axis stepper, shutters, and an emission filter wheel were under software control (MetaMorph, Universal Imaging, Downingtown, PA). Lymph nodes were cemented to the base of the imaging chamber with a thin film of veterinary-grade superglue and were continuously superperfused with warm (35° to 37°C) RPMI 1640 medium bubbled with 95% O_2 and 5% CO_2. For imaging lymphocyte motility, 5D image stacks (*x*, *y*, *z*, time, and emission wavelength) were acquired as follows. Each *xy* plane spanned 200 μm by 200 μm at a resolution of 2 pixels μm^{-1} and was formed by averaging nine video frames. Alternate images at each plane were acquired at emission wavelengths of 510 to 550 nm (for CSFE-labeled cells) and 600 to 700 nm (for CMTMR-labeled cells), selected by a computer-controlled filter wheel. For each time point (10-s intervals), a stack of 17 two-color planes was acquired at axial (*z*) spacings of 3 μm, with a computer-controlled focus motor. After recording, image stacks were processed to yield maximum-intensity projections representing "top" (*xy*) or "side" (*xz*) views through the scanned volume of the lymph node. For single-label experiments with CFSE, excitation at 780 nm provided an optimal signal. For dual-label experiments, the laser was tuned to 820 nm so as to equally excite both fluorophores.
9. K. M. Murphy, A. B. Heimberger, D. Y. Loh, *Science* **250**, 1720 (1990).
10. For antigenic challenge, recipient BALB/c mice were primed by subcutaneous injections with 150 μl of a 1.3% alum emulsion containing 3 μg of ovalbumin and 600 to 800 ng of murine tumor necrosis factor–α (Stemcell Technologies, Vancouver, BC). About 50 μl were injected into three sites on each mouse that were chosen to enhance the delivery of antigen to draining cervical and inguinal lymph nodes. DO11.10 T cells were purified and labeled with CFSE, and 10 million to 12 million $CD3^+$ T cells were adoptively transferred either into antigen-primed mice 24 hours after antigenic challenge or into unprimed recipient mice. At 1 and 5 days after adoptive transfer, the nodes of antigen-primed animals and of unprimed control animals were placed side by side in the recording chamber for sequential imaging.
11. M. Gunzer *et al.*, *Immunity* **13**, 323 (2000).
12. P. Friedl, K. S. Zanker, E. B. Brocker, *Microsc. Res. Tech.* **43**, 369 (1998).
13. P. Friedl, P. B. Noble, E. D. Shields, K. S. Zanker, *Immunology* **82**, 617 (1994).
14. P. A. Negulescu, T. B. Krasieva, A. Khan, H. H. Kerschbaum, M. D. Cahalan, *Immunity* **4**, 421 (1996).
15. C. Elenstrom-Magnusson, W. Chen, B. Clinchy, B. Obrink, E. Severison, *Int. Immunol.* **7**, 567 (1995).
16. J. E. Gretz, C. C. Norbury, A. O. Anderson, A. E. I. Proudfoot, S. Shaw, *J. Exp. Med.* **192**, 1425 (2000).
17. T. E. DeCoursey, K. G. Chandy, S. Gupta, M. D. Cahalan, *J. Gen. Physiol.* **89**, 405 (1987).

18. We thank A. Hejazi for help with cell tracking, L. Forest for care and breeding of the DO11.10 mouse strain, and G. Gutman and G. Chandy for helpful suggestions and comments on the manuscript. Supported by NIH grants GM-48071 (I.P.) and GM-41514 (M.D.C.).

Supporting Online Material

www.sciencemag.org/cgi/content/full/1070051/DC1
Movies S1 to S6

22 January 2002; accepted 12 April 2002
Published online 16 May 2002;
10.1126/science.1070051
Include this information when citing this paper.

Dynamic Imaging of T Cell–Dendritic Cell Interactions in Lymph Nodes

Sabine Stoll,[1] Jérôme Delon,[1] Tilmann M. Brotz,[2]* Ronald N. Germain[1]†

T cell immune responses begin within organized lymphoid tissues. The pace, topology, and outcomes of the cellular interactions that underlie these responses have, so far, been inferred from static imaging of sectioned tissue or from studies of cultured cells. Here we report dynamic visualization of antigen-specific T cells interacting with dendritic cells within intact explanted lymph nodes. We observed immunological synapse formation and prolonged interactions between these two cell types, followed by the activation, dissociation, and rapid migration of T cells away from the antigenic stimulus. This high-resolution spatiotemporal analysis provides insight into the nature of cell interactions critical to early immune responses within lymphoid structures.

Naïve T lymphocytes circulate through the blood and lymph between sojourns within secondary lymphoid tissues (*1*), where they scan peptide–major histocompatibility complex molecule (p-MHC) ligands displayed on the plasma membranes of dendritic cells (DCs) (*2*). If accompanied by appropriate co-signals (*3*), ligand recognition induces T cell clonal expansion together with differentiation that promotes migration either to B cell areas to assist in antibody production (*1*, *4*, *5*) or out of the lymphoid tissue to sites of inflammation (*1*).

Our current view of T cell localization within lymphoid organs and of lymphocyte interaction with antigen-bearing cells derives mainly from static immunohistochemical or fluorescence imaging of cells in tissue sections (*6*) or from static and video microscopic analysis of T cell–antigen-presenting cell (APC) interaction in in vitro models (*7–11*). What is missing is a dynamic, high-resolution view of these events in the more complex, physiological environment of organized lymphoid tissue. To provide this missing information, we have developed a method for extended four-dimensional confocal imaging of T cells and DCs within intact mouse lymph nodes (LNs). In a variation of the technique established by Ingulli *et al.* (*12*), we labeled

[1]Lymphocyte Biology Section, Laboratory of Immunology, National Institute of Allergy and Infectious Diseases, National Institutes of Health, [2]Experimental Immunology Branch, National Cancer Institute, National Institutes of Health, Bethesda, MD 20892, USA.

*Present address: 270 Littlefield Avenue, South San Francisco, CA 94080, USA.

†To whom correspondence should be addressed. E-mail: rgermain@nih.gov

Two-Photon Imaging of Lymphocyte Motility and Antigen Response in Intact Lymph Node

Mark J. Miller *et al.*

Science **296**, 1869 (2002);
DOI: 10.1126/science.1070051